Supporting Information

Constructing Nickel Complex/Crystalline Carbon Nitride Hybrid with a Built-in Electric Field for Boosting CO_2 Photoreduction

Yanrui Li, Linda Wang, Bozhan Li, Liangqing Zhang, Xiaolin Zhu, Xiang Gao**

Y. Li, L. Wang, B. Li, L. Zhang,
College of Materials Science and Engineering
Xi'an University of Science and Technology
Xi'an, 710054, China.

X. Gao
College of Geology and Environment
Xi'an University of Science and Technology
Xi'an 710054, China.

X. Zhu
Key Laboratory of Applied Surface and Colloid Chemistry (Ministry of Education)
School of Chemistry and Chemical Engineering
Shaanxi Normal University
Xi'an,710119

*Corresponding author
E-mail: liyanrui91@xust.edu.cn; gaoxiang@xust.edu.cn

Characterization.

The morphologic structure and element distribution were analyzed using emission scanning electron microscope (SEM) (JSM-7800F, JEOL). X-ray diffraction (XRD) measurements were recorded by a MiniFlex 600 (Rigaku, Japan) with Cu target Kα ray (λ = 0.15406 nm), scanning power (40 kV × 40 mA), scanning range (2θ = 5~60°), scanning speed (10 °C/min). Fourier transform infrared (FTIR) spectra were recorded using the KBr particle technique on the Bruker ALPHA-G spectrometer in Germany. Electrospray ionization high resolution mass spectra (ESI-HRMS) were recorded on Esquire-LC from Bruker with Daltonic Nebulizer 10 psi (dry gas 4 L/min, dry temperature 180 °C). High-resolution transmission electron microscopy images were recorded on transmission electron microscope (JSM-7800F, JEOL). X-ray photoelectron spectroscopy (XPS) data were obtained on a Thermo ESCALAB 250 instrument with a monochromatized Al Ka line source (150 W). All the binding energies were referenced to the C 1s peak at 284.8 eV. The UV-vis diffuse reflection spectrum was measured by the PE lambda 750 instrument of Shimadzu, and solid $BaSO_4$ powder was used as the base material. Steady-state photoluminescence spectra were carried out by (Shimadzu, UV3600) with an incident light of 315 nm. Time-resolved photoluminescence decay spectra were investigated by using Edinburgh S1707092 spectrophotometer with a pulse laser of 375 nm. A diffuse reflectance infrared Fourier transform spectrometer (Bruker TENSOR II) was utilized to explore the *in situ* diffuse reflectance infrared Fourier transformation spectroscopy (DRIFTS) spectra. Before measurement under irradiation, CO_2 flow with water vapor was passed through the sample cell loaded with catalysts powder for 30min.

Ultraviolet photoelectron spectroscopy (UPS) detection: work function (Φ) values of samples were detected by UPS (Themo Scientific, Escalab Xi+) with a He Ⅰ UV source (hv = 21.22 eV), and calculated according to the Equation (1) [1]:

$$\Phi = hv - E_{cutoff} \quad (1)$$

Where the E_{cutoff} referred to high-binding energy secondary electron cutoff.
The valence band (E_{VB}) position was calculated as Equations (2):

$$E_{VB} = hv - (E_{cutoff} - E_{femi}) \quad (2)$$

Where the E_{femi} referred to the energy different between the Fermi level and valence band maximum.

Electrochemical characterization.

The electrochemical measurements were performed using the Shanghai Chenhua CHI760E electrochemical workstation. The standard three-electrode system was adopted in the experiment, with Pt as the counter electrode and Ag/AgCl as the reference electrode. The sample was dissolved in nafion solution and covered on FTO conductive glass as the working electrode. 0.2 M $NaSO_4$ solution as electrolyte. Mott-Schottky (M-S) plots of as-prepared photocatalysts were recorded at 500, 1000, and 1500 Hz under dark condition. The photocurrent measurement was recorded with a 300 W xenon lamp (PLS-SXE300D). Electrochemical impedance spectroscopy (EIS) plots were carried out with the frequency sweep range of 100-106 Hz and the amplitude of 5 mV.

Computational Methods

Density functional theory (DFT) calculations were carried out through the Cambridge Sequential Total Energy Package (CASTEP) code with the generalized gradient approximation (GGA) and Perdew-Burke-Ernzerhof (PBE) functional [2, 3]. The cutoff energy was set to be 435 eV for CCN and 571.4 eV for dcabpyNiBr_2, with Monkhorst-Pack k-point sets of $1 \times 2 \times 1$ for GCN and $1 \times 1 \times 1$ for dcabpyNiBr_2. The convergence criterion for energy and force tolerance were set as 2×10^{-5} eV·atom^{-1} and 0.05 eV·Å^{-1}, respectively. The adsorption energy (E_a) of the adsorbates in CO_2 reduction could be calculated by equation as following [4, 5]:

$$E_a = E_R^* - (E_R + E^*)$$

Where E_R^* was the total energy of an adsorbate (R) adsorbed on the surface (*) and ER and E* are the energies of the single adsorbate and clean surface, respectively.

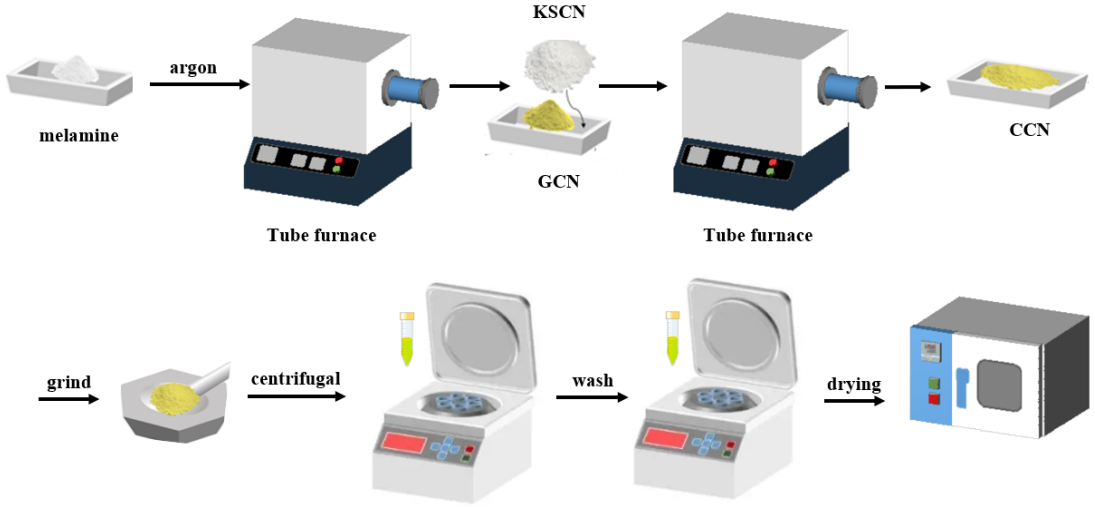

Scheme S1. Experimental preparation flow chart of CCN.

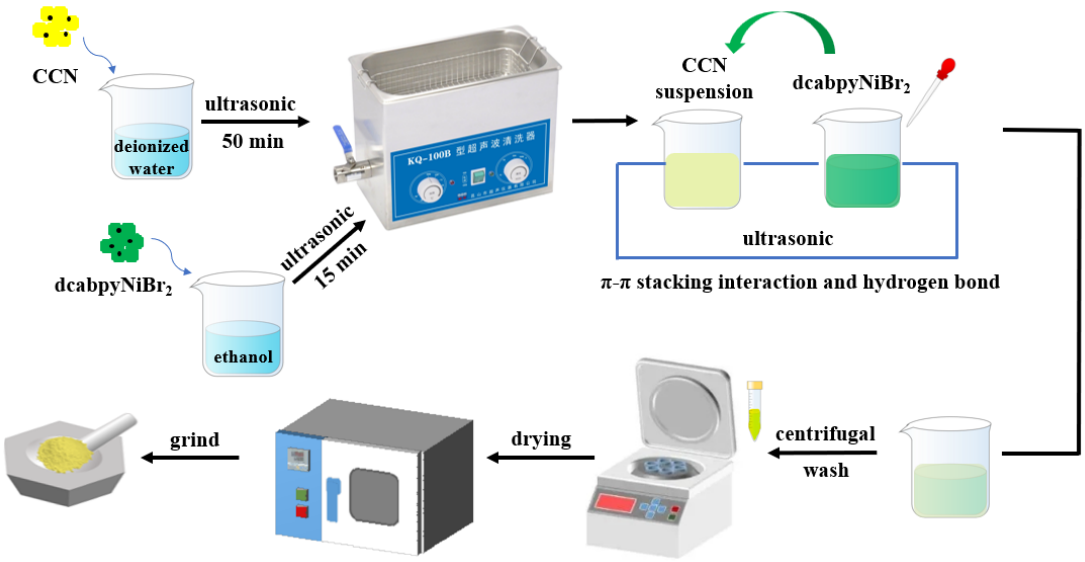

Scheme S2. Experimental preparation flow chart of CCN/Ni*m* hybrids.

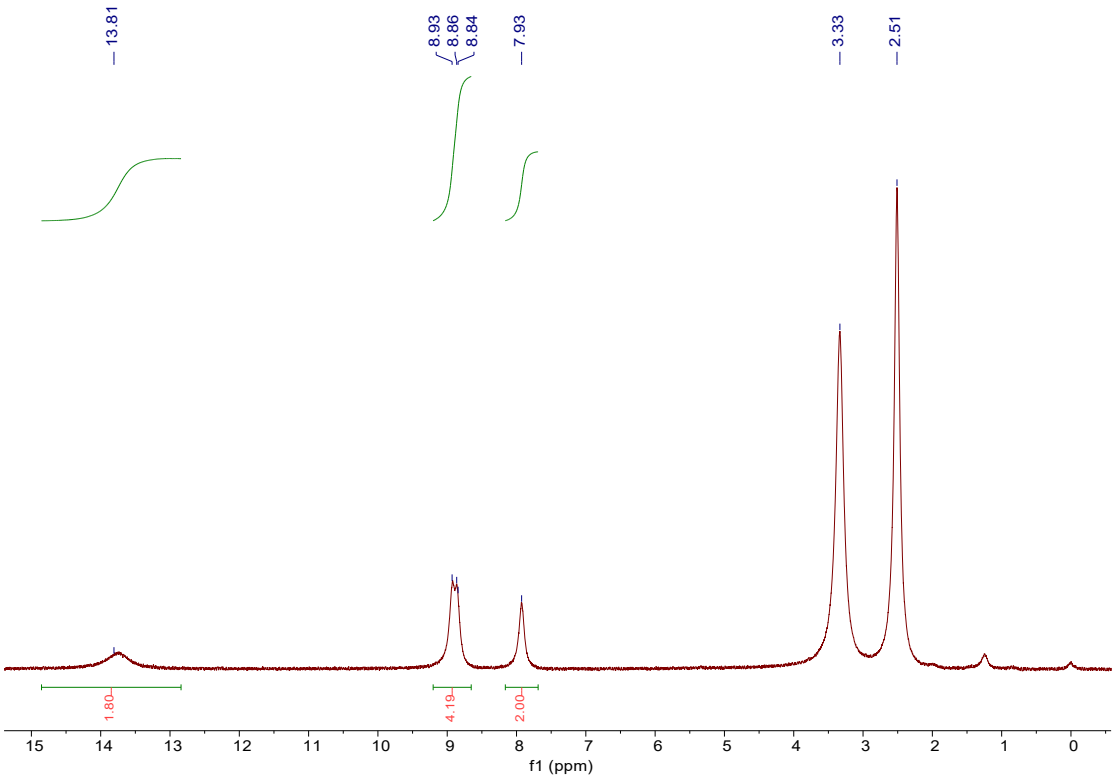

Figure S1. ^{1}H NMR spectrum (400 Mz) of 2,2'-bipyridine-4,4'-dicarboxylic acid in DMSO-d_6.

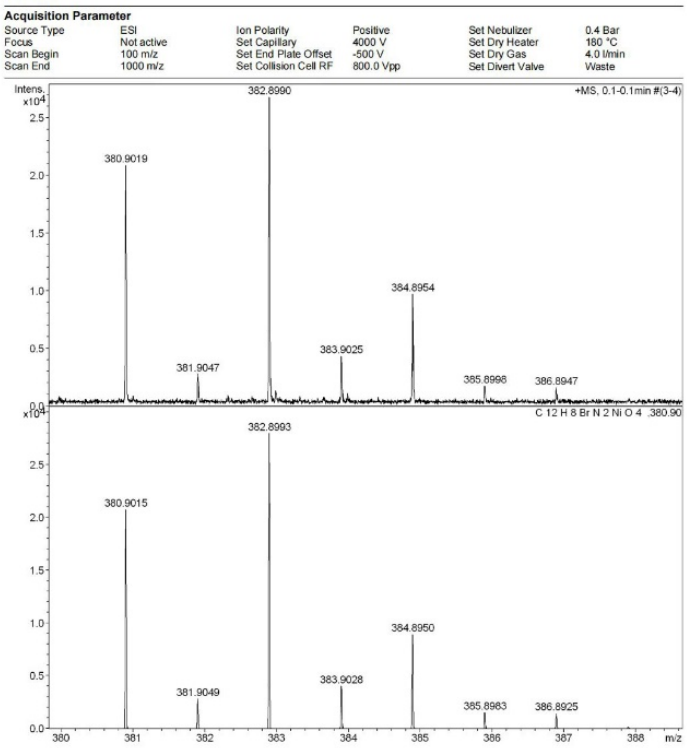

Figure S2. The electrospray ionization high resolution mass spectra (ESI-HRMS) of dcabpyNiBr$_2$.

As illustrated in Figure S3, the UV-visible absorption spectra of ligand (2,2 '-bipyridine-4, 4' -dicarboxylic acids) and dcabpyNiBr$_2$ were recorded in EtOH. The ligand with low solubility in EtOH exhibited an unobvious absorption peak at 300 nm. In contrast to ligand, dcabpyNiBr$_2$ with high solubility in EtOH displayed strengthened absorption intensity and red-shift absorption peak at about 320 nm, attributed to the metal-to-ligand charge transfer (MLCT) [6], which again confirmed the successful synthesis of dcabpyNiBr$_2$.

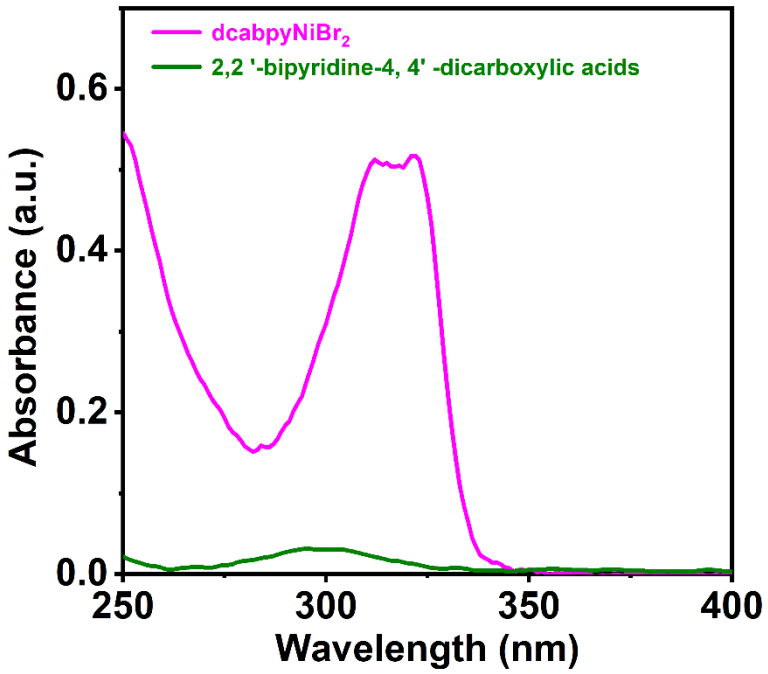

Figure S3. UV-visible absorption spectra of dcabpyNiBr$_2$ and 2,2'-bipyridine-4,4'-dicarboxylic acids in EtOH.

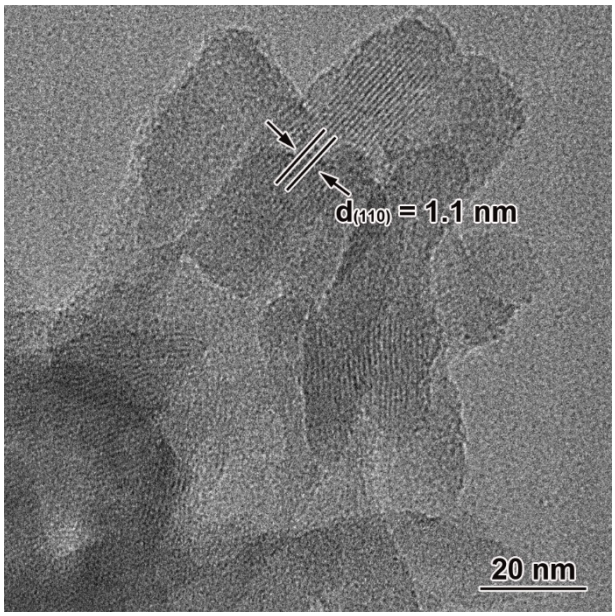

Figure S4. High-resolution transmission electron microscopy (HRTEM) image of CCN.

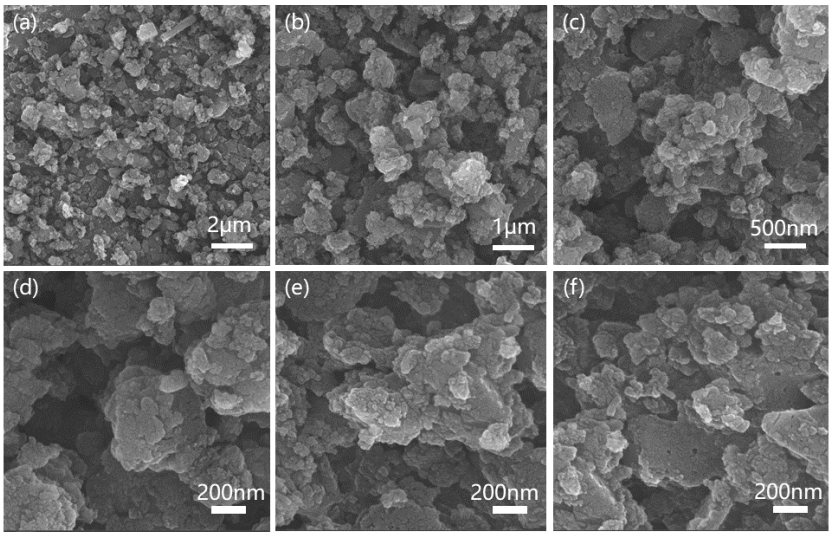

Figure S5. SEM spectra of GCN, CCN, CCN/Ni-1, CCN/Ni-5, CCN/Ni-10 and CCN/Ni-15.

The surface atomic ratios of carbon to nitrogen (C:N) in GCN were measured by XPS to be about 3:3.689, close to the value of the stoichiometric carbon nitride (3:4) (Figure S6a, Table S2). As shown in Figure S6b, two C 1s XPS peak at 284.8 eV and 288.1 eV indexed to graphitic carbon and the sp^2-bonded carbon in aromatic ring (N=C-N) could be detected from GCN [7]. Three peaks at 398.4 eV, 399.8 eV, and 401.0 eV could be found in the N 1s spectrum of GCN, corresponding to triangular edge nitrogen, central tertiary nitrogen and amino groups [8] (Figure 63c), respectively.

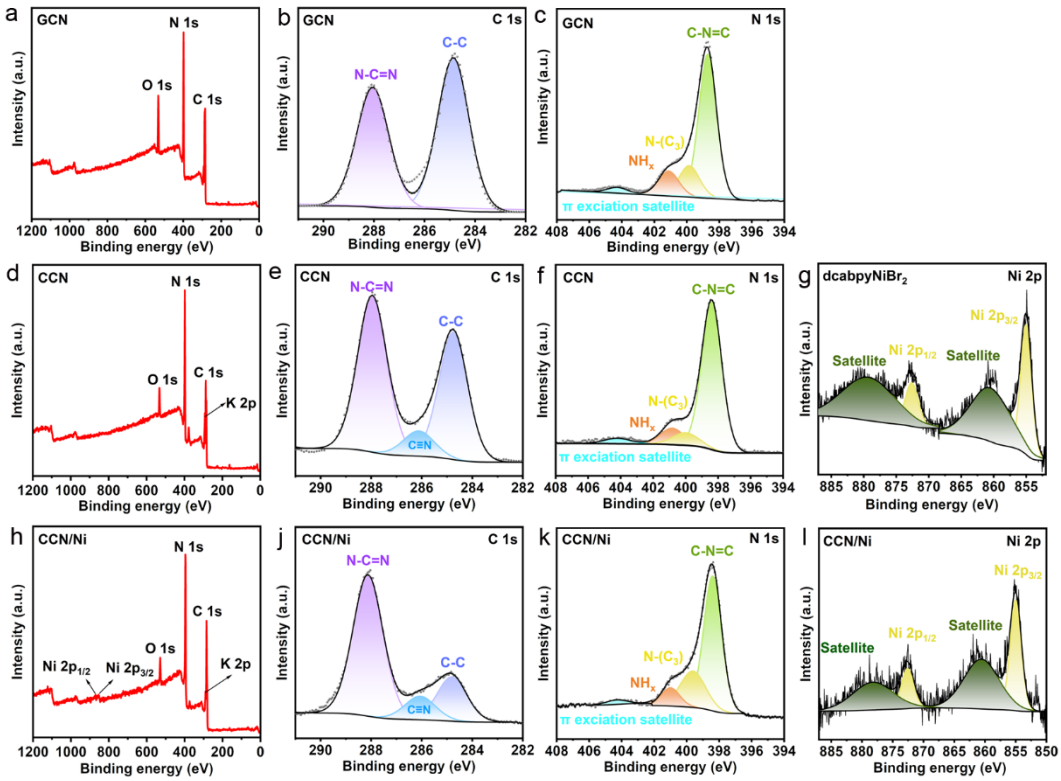

Figure S6. XPS pattern of GCN, CCN and CCN/Ni-10. (a) XPS survey spectrum of GCN. XPS spectra of (b) C 1s, (c) N 1s of GCN. (d) XPS survey spectrum of CCN. XPS spectra of (e) C 1s, (f) N 1s of CCN. and (g) Ni 2p of dcabpyNiBr$_2$. (h) XPS survey spectrum of CCN/Ni-10. XPS spectra of (j) C 1s, (k) N 1s, and (i) Ni 2p of CCN/Ni-10.

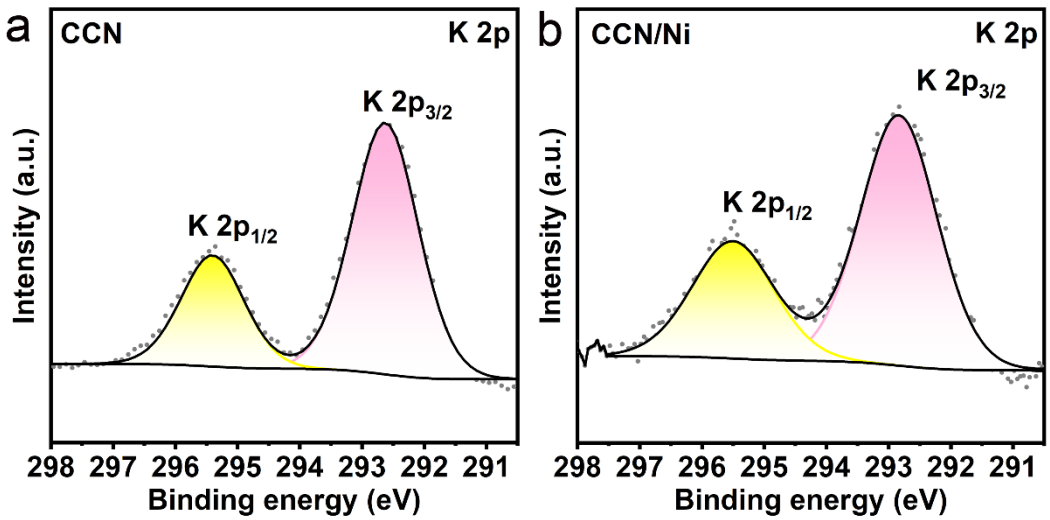

Figure S7. XPS pattern. XPS pattern of (a) K 2p of CCN and (f) CCN/Ni.

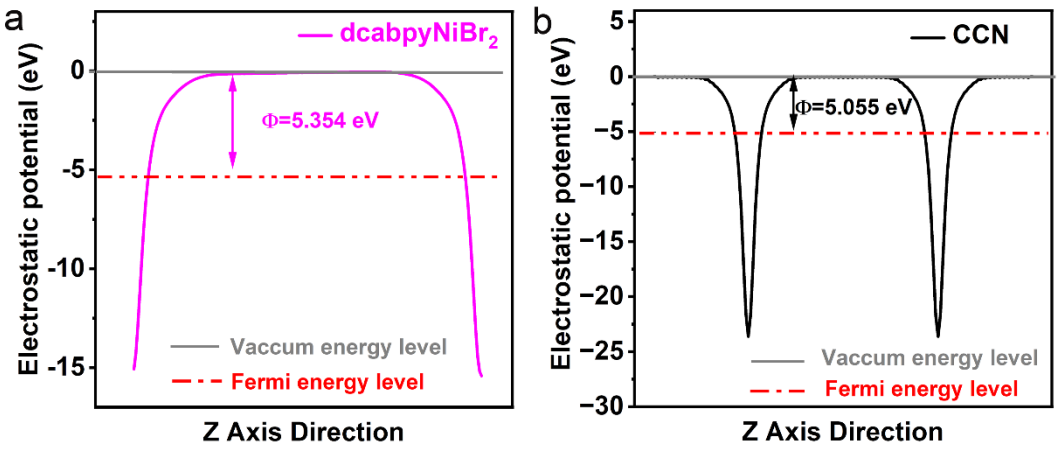

Figure S8. Electrostatic potentials for a) dcabpyNiBr$_2$ and b) CCN.

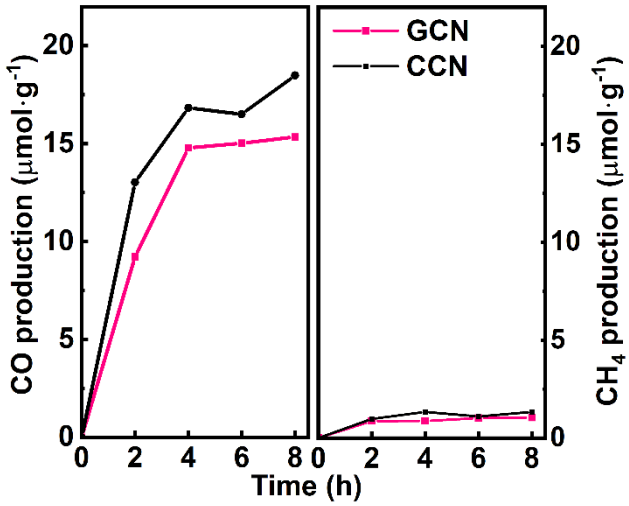

Figure S9. CO and CH_4 evolution with irradiation times for GCN and CCN.

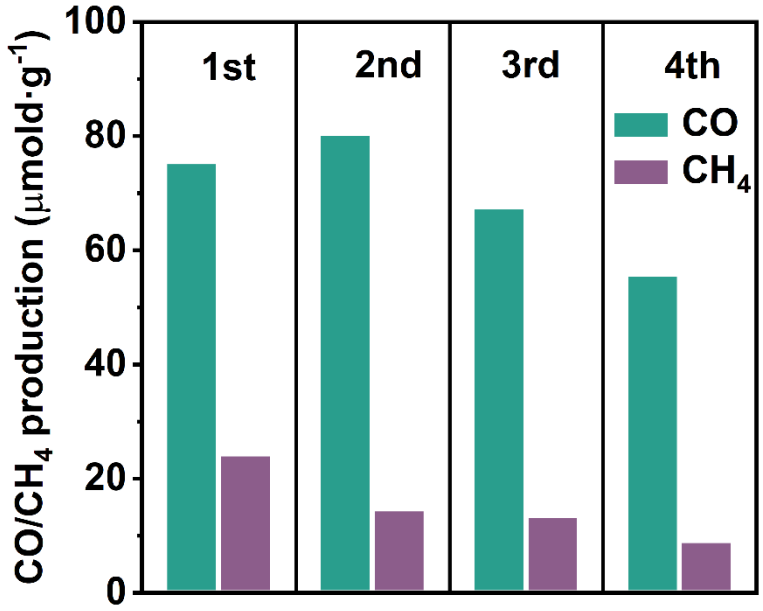

Figure S10. Recycling tests of time dependent CO and CH_4 production over CCN/Ni-10 during 8 h for each run.

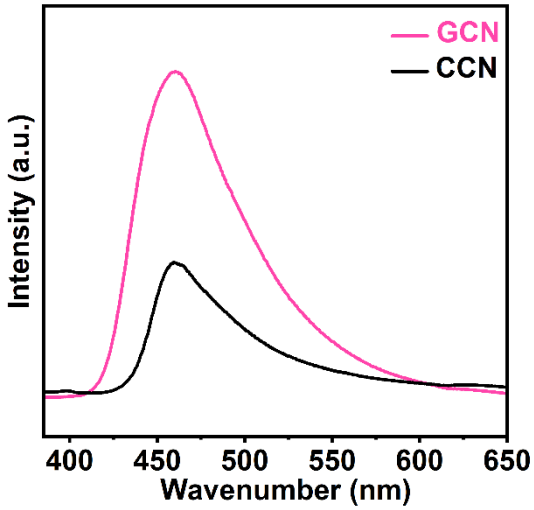

Figure S11. Steady-state photoluminescence spectra for GCN and CCN.

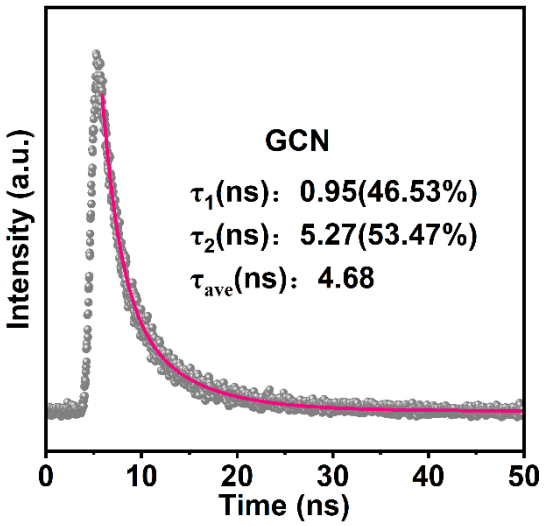

Figure S12. Time-resolved photoluminescence spectra for GCN.

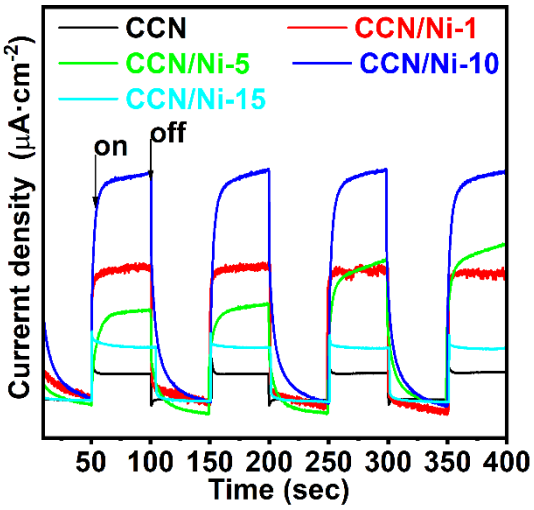

Figure S13. Photocurrents for CCN and CCN/Ni*m* hybrids.

Table S1. Layer spacing and full width at half maximum (FWHM) were obtained from the (002), (100), (020), and (110) peaks in XRD patterns of GCN, CCN, and CCN/Ni*m* hybrids.

	GCN	CCN	CCN/Ni-1	CCN/Ni-5	CCN/Ni-10	CCN/Ni-15
FWHM	1.33	1.17	0.86	0.85	0.89	0.75
d_{002} (Å)	3.23	3.20	3.18	3.18	3.17	3.15
d_{100} (Å)	6.75	/	/	/	/	/
d_{020} (Å)	/	8.75	8.75	8.75	8.75	8.75
d_{110} (Å)	/	11.04	11.04	11.04	11.04	11.04

Table S2. Surface element percentages of GCN, CCN and CCN/Ni-10 by XPS. C1, C2, and C3 are related to graphitic carbon, sp^2-bonded carbon in the aromatic ring (N=C-N) and sp^3-bonded carbon in -C≡N groups, respectively, as displayed in Figure S6a and S6e.

Sample	O (at%)	C (at%)			N (at%)	K (at%)	Ni (at%)	C : N Atomic ratio
GCN	6.33	60.84			32.83	0	0	3:3.689
		C1 (at%)	C2 (at%)	C3 (at%)				
		56.11	43.89	0				
CCN	3.58	50.21			33.05	14.16	/	3:3.643
		C1 (at%)	C2 (at%)	C3 (at%)				
		45.78	45.15	9.07				
CCN/Ni-10	3.26	50.74			33.07	12.78	0.14	/

a. at% is the atomic percentage;

b. C : N atomic is calculated by C : N = (C × (C2+C3)): N, by excluding the inevitable graphitic carbon (C1) originating from surrounding or contaminants.

c. Given CCN/Ni-10 composed of CCN and dcabpyNiBr_2, it is difficult to exclude the O, C, and N elements from dcabpyNiBr_2. Thus, the C: N value for CCN/Ni-10 calculated by equation b is inaccurate.

Table S3. The interface charge transfer resistances and CPE of CCN, CCN/Ni-1, CCN/Ni-5, CCN/Ni-10 and CCN/Ni-15.

	CCN	CCN/Ni-1	CCN/Ni-5	CCN/Ni-10	CCN/Ni-15
R_s (Ω cm^2)	4.28	4.66	2.17	1.07	3.71
R_{ct} (Ω cm^2)	47.13	21.18	15.74	5.02	33.75
CPE (S^n Ω^{-1} cm^{-2})	1.57×10^{-8}	4.68×10^{-8}	6.47×10^{-8}	4.44×10^{-9}	1.77×10^{-8}

References

[1] L. Zhai, X. She, L. Zhuang, Y. Li, R. Ding, X. Guo, Y. Zhang, Y. Zhu, K. Xu, H. J. Fan, S. P. Lau, *Angew. Chem. Int. Ed.* 2022, **61**, e202116057.

[2] S. J. Clark, M. D. Segall, C. J. Pickard, P. J. Hasnip, M. I. J. Probert, K. Refson, M. C. Payne, *Cryst. Mater.*, 2005, **220**, 567.

[3] M. Segall, P. Lindan, M. Probert, C. Pickard, P. Hasnip, S. Clark, M. Payne, *J. Phys.: Condens. Matter* 2002, **14**, 2717.

[4] G. Li, J. Han, H. Wang, X. Zhu, Q. Ge, *ACS Catal.* 2015, **5**, 2009.

[5] Y. Wu, C. Li, W. Liu, H. Li, Y. Gong, L. Niu, X. Liu, C. Sun, S. Xu, *Nanoscale* 2019, **11**, 5064.

[6] M. C. Rosko, K. A. Wells, C. E. Hauke, F. N. Castellano, *Inorg. Chem.*, 2021, **60**, 8394-8403.

[7] W. Lei, D. Portehault, R. Dimova, M. Antoniettit, *J. Am. Chem. Soc.* 2011, **133**, 7121.

[8] Y. Li, Y. Wang, C. L. Dong, Y. C. Huang, J. Chen, Z. Zhang, F. Meng, Q. Zhang, Y. Huangfu, D. Zhao, L. Gu and S. Shen, *Chem. Sci.* 2021, **12**, 3633.